

Supplementary information

Methods

Elevation data. We use surface elevation data between 07/2010 and 07/2017 from the SAR Interferometric Radar Altimeter (SIRAL) onboard the European Space Agency (ESA) CryoSat-2 satellite (Wingham et al., 2006). SIRAL is a beam-forming active microwave radar altimeter with a maximum imaging range of ~15 km on the ground. The sensor emits time-limited *Ku-band* pulses aimed at reducing the footprint to ~1.6 km within the beam. Over Arctic GIC, the sensor operates in synthetic aperture interferometric (SARIn) mode, which allows delay-Doppler processing to increase the along-track resolution to ~380 m, while cross-track interferometry is used to extract key information about the position of the footprint centre. CryoSat-2 orbits the Earth with a 369-day repeat period formed by the successive shift of a 30-day sub-cycle. The satellite has an inclination of 92°, offering complete coverage of the Arctic GIC and a rapid increase in orbit cross-over density towards the poles - from 7.5 km inter-track distance at the Equator to less than 1.6 km at latitudes higher than 70° (Wingham et al., 2006).

Swath processing. We process *level 1b*, baseline C data supplied by the ESA ground segment using a swath processing algorithm. *Level 1b* data is provided as a sequence of radar echoes along the satellite track, which translates into single power, interferometric phase and coherence waveforms for each along-track location (Gourmelen et al., 2018). The conventional *level 1b* data processing method consists in extracting single elevation measurements from the power signal in each waveform that corresponds to the Point of Closest Approach (POCA) between satellite and the ground. In contrast, swath altimetry exploits the full radar waveform to map a dense swath (~5km wide) of elevation measurements across the satellite ground track beyond POCA (Gray et al., 2013; Gray et al., 2015; Foresta et al., 2016; Ignézi et al., 2016; Christie et al., 2016; Gourmelen et al., 2018; Foresta et al., 2018) providing one to two orders of magnitude more elevation measurements compared with POCA. This makes the CryoSat-2 sensor at present the only radar altimeter able to measure routinely small GIC at high resolution.

Gridded topography and elevation change. Gridded elevation is computed using a plane-fit algorithm for the entire measurement period, 2010-2017. The dense elevation field $h(x, y, t)$ allows gridding with a cell resolution of 500m. The measurements sampled within 500 m from each pixel centre (x_p, y_p) are expressed as a function of easting (x), northing (y), and time (t):

$$h(x, y, t) = c_0 x + c_1 y + c_2 t + c_3 = \nabla h(x, y) + \dot{h}t + c$$

where

$$\nabla h(x, y) = \frac{\partial h}{\partial x}x + \frac{\partial h}{\partial y}y \quad \text{and} \quad \dot{h} = \frac{\partial h}{\partial t}$$

$\nabla h(x, y)$ is the ice surface gradient, and the time-dependent coefficient c_2 retrieved from the linear fit is the rate of surface elevation change \dot{h} . The gridded elevations $h_p(x_p, y_p)$ are fitted to the measurement field around each pixel centre using an iterative 3 σ -filter at each step until all outliers are removed (Foresta et al., 2016).

Validation. We compare CryoSat-2 gridded \dot{h} at 500 m posting with airborne records from the NASA Operation Ice Bridge (OIB) Airborne Topographic Mapper (ATM). We were able to locate two single validation test sites in the Arctic beyond Greenland with measurements sampled after the launch of CryoSat-2: Barnes Ice Cap on Baffin Island, and Devon Ice Cap on Devon Island, Canadian High Arctic (Supplementary Figure S4). The data drawn for comparison is NASA IceBridge ATM L4 Surface Elevation Rate of Change, Version1 (Studinger, 2014), sampled along extensive OIB repeat flight paths

in 2010 and 2015. We match these data with \dot{h} generated from CryoSat-2 measurements acquired between 2010 and 2015. The validation is constrained to OIB measurements that are within 250 m of the CryoSat-2 \dot{h} grid centre (1/2 grid spacing). We calculate a measurement bias as the median value of the difference between swath products and OIB measurements (that is, CS-2 swath minus OIB). Validation of rates of \dot{h} yields a minimal bias of $0.05 \text{ m a}^{-1} \pm 0.26 \text{ m a}^{-1}$ and $0.00 \text{ m a}^{-1} \pm 0.13 \text{ m a}^{-1}$ respectively for Barnes and Devon Ice Caps (Supplementary Figure S4). The small difference can arise from differences in spatial and temporal resolutions and/or signal properties. We also inspected elevation time-series to ensure that rates of change were not affected by spurious elevation biases related to changes in the scattering horizon (Nilsson et al., 2016; Slater et al., 2019). A more complete validation exercise of CryoSat-2 swath products was performed by Gourmelen et al. (2018) over parts of the Greenland- and Antarctic Ice Sheets.

Ice and snow masks. We use ice and snow masks to delimit the regions covered in ice from bare ground and ocean water in all gridded products. The masks are also used to differentiate between pixels pertaining to land- versus marine-terminating basins. They are retrieved in vector (*shp*) format from the Randolph Glacier Inventory (RGI) 6.0, available at Global Land Ice Measurements from Space (GLIMS). Partitioning between land- and marine-terminating basins needed to be corrected for misallocations in RGI 6.0 for some regions. Most substantial adjustments were made for Sv, where a number of land-terminating basins needed to be re-allocated as marine-terminating based on visual inspection of online maps from the Norwegian Polar Institute available at www.npolar.no. Reallocation was made for the following GIC basins/ glaciers: Augnebreen, Aldousbreen, Besselsbreen, Bragebreen, Deltabreen, Duckwitzbreen, Fjortende Julibreen, Franklinbreen N and S, Frazerbreen, Gimlebreen, Hayesbreen, Hochstetterbreen, Idunbreen, Infantfonna, Ingerbreen, Innifonna, Johansenbreen, Kongsbreen, Kongsvegen, Kronebreen, Mittag-Lefflerbreen, Monacobreen, Negribreen, Nordenskiöldbreen, Nordsysselebreen, Oslobreen, Paulabreen, Petermannbreen, Polarisbreen, Recherchebreen, Scheibreen, Sidevegen, Spælbreen, Stonebreen, Tunabreen, Vaigattbreen.

The following Arctic sub-regions are covered by GIC but were not included in this study as CryoSat-2 does not operate in SARIn mode at their location (see CryoSat-2 Geographical Mode Mask, <https://earth.esa.int/web/guest/-/geographical-mode-mask-7107>, accessed on 02/04/2019): Jan Mayen, Kvitøya Ice Cap (Sv), Victoria Ice Cap (FJL), Ushakov Ice Cap (Ushakov Island, RAA), Schmidt Ice Cap (SZ). Together these ice masses extend over a relatively small glaciated area ($\sim 1600 \text{ km}^2$). The De Long Islands ice caps (East-Siberian Sea, RAA) were also excluded due to their small size (total glaciated area $< 80 \text{ km}^2$ (Glazovski, 1996)). For all regions, we assume that during the period of measurement the glaciated area remains constant.

Volume change. We use surface elevation changes from our gridded \dot{h} maps to calculate volume change rates \dot{V} over the entire Arctic between 2010 and 2017. Volumetric changes are computed as the sum of the gridded surface elevation change rates from each pixel of a denoised gridded \dot{h} product multiplied by the pixel area as defined by the posting ($0.5 \times 0.5 \text{ km}^2$ per pixel):

$$\dot{V}_{denoised} = A_{pixel} \cdot \sum \dot{h}_{denoised}$$

Denoising is performed for each region separately by removing pixels with values of $|\dot{h}| > \delta$, and errors on \dot{h} above a certain threshold. We choose $\delta = 25 \text{ m a}^{-1}$ and $\delta = 50 \text{ m a}^{-1}$ for land- and marine-terminating basins, respectively, as the maximum realistic rates of change. Errors on \dot{h} are extracted from the covariance matrix of the plain-fit algorithm used to compute gridded elevations (Foresta et al., 2016). We select an appropriate error threshold by iteratively computing $\dot{V}_{denoised}$ while increasing the allowed maximum error on \dot{h} at each step until $\dot{V}_{denoised}$ converges towards a plateau value. The

final error threshold is chosen so that the number of outliers is minimised after $\dot{V}_{denoised}$ converges. \dot{h} error thresholds vary between $3 \pm 2 \text{ m a}^{-1}$ and are specific for each region.

To calculate the total volume change \dot{V} , we make assumptions about areas not covered by measurements or where outliers were removed. For the land-terminating segments, where we assume that *SMB* processes are largely dominating the overall mass budget, we fill the data gaps by applying hypsometric averaging (Foresta et al., 2016, 2018) (Table S1). This approach is not applicable for marine-terminating basins however, where dynamic processes often lead to significant geometric changes over the ice surface, and hence, a simple relationship between \dot{h} and elevation is not sufficient to describe volume loss. Thanks to the high density of observations provided by CryoSat-2 (Supplementary Table S1), particularly for the marine-terminating sectors of FJL, NZ, SZ, and Sv, we rescale $\dot{V}_{denoised}$ using the ratio of total-to-measured glaciated area:

$$\dot{V} = \frac{n_{total}}{n_{denoised}} \cdot \dot{V}_{denoised}$$

where n_{total} is the total number of pixels and $n_{denoised}$ the number of pixels in the denoised \dot{h} product.

We performed a sensitivity test of the upscaling method by comparing against hypsometric averaging over the land-terminating segments of single CAA ice caps (Table S1). Both CAA-N and CAA-S are characterised by rugged topography and are the regions with lowest data coverage. The comparison reveals little difference in the mass budget between the two regionalisation schemes. We therefore apply upscaling as a method to fill data gaps in the marine-terminating segments of all Arctic GIC, including CAA-S and CAA-N.

Mass change. The conversion from volume- to mass change is performed using a constant density of ice ρ_{ice} equal to $850 \pm 60 \text{ kg m}^{-3}$ as advocated by Huss (2013) to better account for a wide range of surface conditions (Table S1). For each of the seven regions in Table 1 we apply the appropriate regionalisation scheme to the sum of all land- and marine-terminating basins separately, and compute the corresponding land- and marine-terminating mass budgets (\dot{m}_l and \dot{m}_m , respectively). The total mass balance \dot{m} is then calculated as the sum of the two segments:

$$\dot{m} = \dot{m}_l + \dot{m}_m$$

Computing mass budgets on a single ice cap basis brings insignificant changes to the overall result (Supplementary Table S1), with differences well within error margins. For the CAA this confirms similar findings Gardner et al., (2011). Specific mass balance is calculated as the ratio of mass change to surface area, whereby the glaciated area extent is based on the glacier outlines from RGI 6.0.

Partitioning total mass balance into *SMB* and *D*. Local elevation changes over the ice surface occur as a result of anomaly in surface mass balance (*SMB*) and anomaly in ice discharge (*D*), and are described by the kinematic relation for \dot{h} (Cuffey and Paterson, 2010). To quantify the relative contribution of *SMB* and *D* to the overall mass loss, we parametrize thinning \dot{h} as a function of elevation (h_l), and spatial coordinates (x_l , y_l) over land-terminating GIC basins only for each of the seven regions listed in Table 1:

$$\dot{h}_l \approx a_0 h_l^3 + a_1 h_l^2 + a_2 h_l + a_3 x_l + a_4 y_l + a_5$$

The function describes the direct influence of elevation, latitude and longitude on *SMB*-related elevation change \dot{h}_l . We use the coefficients a_i and gridded elevations $h_l(x_l, y_l, t)$ and $h_m(x_m, y_m, t)$ over

land- and marine-terminating sectors, respectively, to calculate parametrised area-specific bulk SMB_{l,p_spec} and SMB_{m,p_spec} , separately for both types of basins:

$$SMB_{l/m,p_spec} = \frac{A_{pixel}}{A_{l/m}} \cdot \rho_{ice} \cdot \sum \dot{h}_{l/m,p}$$

where

$$\dot{h}_{l/m,p} = a_0 h_{l/m}^2 + a_1 h_{l/m} + a_2 x_{l/m} + a_3 y_{l/m} + a_4$$

A_l and A_m are the total surface area of land- and marine- terminating basins, respectively. Using parametrised $SMB_{l/m,p_spec}$, we derive bulk marine-terminating area-specific SMB_{m_spec} as follows:

$$SMB_{m_spec} = \frac{SMB_{l_spec}}{r}$$

where

$$r = \frac{SMB_{l,p_spec}}{SMB_{m,p_spec}}$$

We then calculate D by subtracting SMB_{m_spec} from the total specific mass balance \dot{m}_{m_spec} and by multiplying the result by the total area A_m of marine-terminating GIC basins. To evaluate our parametrisation of \dot{h}_l we calculate the root mean square error (RMSE) of the polynomial fit as:

$$RMSE = \sqrt{\frac{\sum (\dot{h}_{l,p} - \dot{h}_l)^2}{n}}$$

where n is the number of grid cells. RMSE values vary regionally and range between 0.53 m a^{-1} and 6.41 m a^{-1} .

SMB comparison CryoSat-2 - RACMO2.3. To evaluate our method for partitioning mass imbalance into SMB and D , we use seven glaciological years (10/2010 - 09/2017) of monthly area-specific SMB data for CAA-N and CAA-S from the Regional Climate Model RACMO2.3. The dataset and the corresponding ice masks are down-sampled to 1km (Noel et al., 2018). We produce additional ice masks at 1km resolution for marine- and land-terminating basins separately for both CAA-N and CAA-S based on the RGI 6.0 split between the two types of basins. Annual SMB is calculated pixelwise for each year and then integrated over the entire area to obtain total SMB by region and terminus type.

Error budget. The uncertainty associated with the calculated mass imbalance is the result of unknown density fluctuations, gradients in snow accumulation, and errors in elevation trends from the satellite measurements. The elevation measurement errors can be attributed to instrument system errors (intrinsic to *Level 1b* data) on one hand, and to retracking errors in the swath processing algorithm on the other hand. We estimate a representative uncertainty of the mass imbalance, using the same method as in Foresta et al., (2016 and 2018). We account for errors in the measurement statistically by extracting from the covariance matrix of our surface elevation fit the variances $\varepsilon_{\dot{h}}$ that are assigned to the rates of \dot{h} . Depending on the type of drainage basin the error on volume change $\varepsilon_{\dot{V}}$ is obtained by propagating $\varepsilon_{\dot{h}}$ either by hypsometric averaging (land-terminating basins), or rescaling by the ratio of total-to-measured surface area (marine-terminating basins). For the volume-to-mass conversion we assume a constant error on the density $\varepsilon_{\rho} = 60 \text{ kg m}^{-3}$ following Huss (2013). The error on the mass imbalance is calculated using uncorrelated Gaussian error propagation as:

$$\varepsilon_{\dot{m}} = |\dot{m}| \cdot \sqrt{\left(\frac{\varepsilon_{\dot{V}}}{\dot{V}}\right)^2 + \left(\frac{\varepsilon_{\rho}}{\rho_{ice}}\right)^2}$$

For land-terminating drainage basins we assume that $\varepsilon_{\dot{m}} = \varepsilon_{SMB}$. *SMB* uncertainties of marine-terminating basins are estimated by assigning the root mean square deviation of our *SMB* parametrisation to the error $\varepsilon_{\dot{h}}$ on \dot{h} and applying Gaussian error propagation as described above. For *D* we derive uncertainties ε_D from the quadrature of $\varepsilon_{\dot{m}}$ and ε_{SMB} :

$$\varepsilon_D = \sqrt{(\varepsilon_{\dot{m}})^2 + (\varepsilon_{SMB})^2}$$

Climate data analysis. We use global Arctic maps of 2 m air temperature (T_{2m}) and sea surface temperature (SST) provided on a 0.75° and averaged into monthly means from ECMWF Interim Re-Analysis (ERA-I)⁶² with the smallest bias from observations (Lindsay et al., 2014). The 200 m depth subsurface ocean temperature (SOT) from TOPAZ (Xie et al., 2017) reanalysis in the Arctic is provided on a 12-16 km grid and analysed for the 15th day of each month. The passive microwave NASA Team (Cavalieri et al., 2019) and Bootstrap (Comiso, 2017) sea ice concentration (SIC) data are monthly means on a 25 km by 25 km polar stereographic grid.

Regional averages surrounding each GIC (values on Table 3) are calculated by nearest neighbor interpolation from the native grids of each forcing data to the target regions shown in Figure 1. For T_{2m} , we compute the average over each GIC location including adjacent non-GIC areas of land and ocean.

References

51. Wingham, D. J. *et al.* CryoSat: A mission to determine the fluctuations in Earth's land and marine ice fields. *Adv. Sp. Res.* **37**, 841–871 (2006).
52. Gray, L. *et al.* CryoSat-2 delivers monthly and inter-annual surface elevation change for Arctic ice caps. *Cryosph.* **9**, 1895–1913 (2015).
53. Wingham, D. J., Siegert, M. J., Shepherd, A. & Muir, A. S. Rapid discharge connects Antarctic subglacial lakes. *Nature* **440**, 1033–1036 (2006).
54. Gray, L. *et al.* Interferometric swath processing of Cryosat data for glacial ice topography. *Cryosphere* **7**, 1857–1867 (2013).
55. Ignécz, Á. *et al.* Northeast sector of the Greenland Ice Sheet to undergo the greatest inland expansion of supraglacial lakes during the 21st century. *Geophys. Res. Lett.* **43**, 9729–9738 (2016).
56. Christie, F. D. W., Bingham, R. G., Gourmelen, N., Tett, S. F. B. & Muto, A. Four-decade record of pervasive grounding line retreat along the Bellingshausen margin of West Antarctica. *Geophys. Res. Lett.* **43**, 5741–5749 (2016).
57. Studinger, M. *IceBridge ATM L4 Surface Elevation Rate of Change, Version 1.* (2014).
58. Nilsson, J., Gardner, A., Sørensen, L. S. & Forsberg, R. Improved retrieval of land ice topography from CryoSat-2 data and its impact for volume-change estimation of the Greenland Ice Sheet. *Cryosphere* **10**, 2953–2969 (2016).
59. Glazovski, A. F. *Mass Balance of Arctic Glaciers, IASC Report No. 5.* (1996).
60. Foresta, L. *et al.* Heterogeneous and rapid ice loss over the Patagonian Ice Fields revealed by CryoSat-2 swath radar altimetry. *Remote Sens. Environ.* **211**, 441–455 (2018).
61. Cuffey, K. M. & Paterson, W. S. B. *The Physics of Glaciers.* (Elsevier, 2010).
62. Dee, D. P. *et al.* The ERA-Interim reanalysis: Configuration and performance of the data assimilation system. *Q. J. R. Meteorol. Soc.* **137**, 553–597 (2011).
63. Lindsay, R., Wensnahan, M., Schweiger, A. & Zhang, J. Evaluation of seven different atmospheric reanalysis products in the Arctic*. *J. Clim.* **27**, 2588–2606 (2014).
64. Xie, J., Bertino, L., Knut, L. & Sakov, P. Quality assessment of the TOPAZ4 reanalysis in the Arctic over the period 1991–2013. *Ocean Sci.* **13**, 123–144 (2017).
65. Cavalieri, D., Parkinson, C., Gloersen, P. & Zwally, J. H. *Sea ice concentrations from Nimbus-7 SMMR and DMSP SSM/I-SSMIS passive microwave data, Version 1.* (2019).
66. Comiso, J. C. *Bootstrap sea ice concentrations from Nimbus-7 SMMR and DMSP SSM/I-SSMIS, Version 3.* (2017).
67. Moholdt, G., Nuth, C., Hagen, J. O. & Kohler, J. Recent elevation changes of Svalbard glaciers derived from ICESat laser altimetry. *Remote Sens. Environ.* **114**, 2756–2767 (2010).
68. Nilsson, J., Sørensen, L. S., Barletta, V. R. & Forsberg, R. Mass changes in Arctic ice caps and glaciers: Implications of regionalizing elevation changes. *Cryosph.* **9**, 139–150 (2015).
69. Schrama, E. J. O. & Wouters, B. Revisiting Greenland ice sheet mass loss observed by GRACE. *J. Geophys. Res.* **116**, 1–10 (2011).
70. Jacob, T., Wahr, J., Pfeffer, W. T. & Swenson, S. Recent contributions of glaciers and ice caps to sea level rise. *Nature* **482**, 514–518 (2012).
71. Colgan, W. *et al.* Hybrid glacier Inventory, Gravimetry and Altimetry (HIGA) mass balance product for Greenland and the Canadian Arctic. *Remote Sens. Environ.* **168**, 24–39 (2015).
72. Box, J. E. *et al.* Global sea level contribution from Arctic land ice: 1971–2017. *Environ. Res. Lett.* **13**, 125012 (2018).
73. Schrama, E. J. O., Wouters, B. & Rietbroek, R. A mascon approach to assess ice sheet and glacier mass balances and their uncertainties from GRACE data. *J. Geophys. Res. Solid Earth* **119**, 6048–6066 (2014).
74. Bamber, J. L., Westaway, R. M., Marzeion, B. & Wouters, B. The land ice contribution to sea level during the satellite era (2018 Environ. Res. Lett. 13 063008). *Environ. Res. Lett.* **13**, 099502 (2018).
75. Harcourt, W. D. *et al.* Subglacial controls on dynamic thinning at Trinity- Wykeham Glacier , Prince of Wales Ice Field , Canadian Arctic. *Int. J. Remote Sens.* **00**, 1–23 (2019).

Figures

Table S1 | Mass balance of Arctic GIC: split by type of basin (marine- and land-terminating), comparison of upscaling (S) versus hypsometric averaging (H) as regionalisation schemes of land-terminating basins.

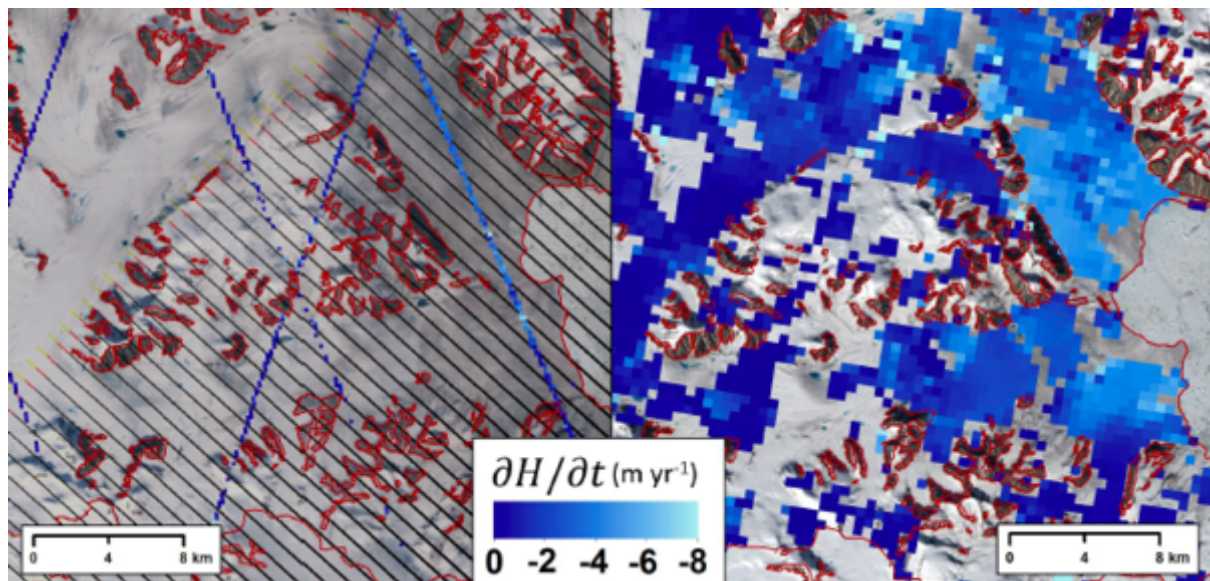
Region / GIC	Total MB	Marine-terminating basins		Land-terminating basins		
	[Gt a ⁻¹]	S [Gt a ⁻¹]	A _{measured} / A _{total}	S [Gt a ⁻¹]	H [Gt a ⁻¹]	A _{measured} / A _{total}
FJL	-3.8 ± 0.3	-3.7 ± 0.3	90%	-0.2 ± 0.0	-0.1 ± 0.0	88%
Windy	+0.3 ± 0.0	+0.2 ± 0.0	86%	+0.1 ± 0.0	+0.1 ± 0.0	82%
NZ	-8.5 ± 0.4	-5.2 ± 0.4	83%	-3.0 ± 0.2	-3.3 ± 0.2	70%
SZ	-1.7 ± 0.1	-1.6 ± 0.1	90%	0.1 ± 0.0	-0.1 ± 0.0	82%
Sum GIC and upscale	-1.7 ± 0.1	-1.6 ± 0.1		0.1 ± 0.0	-0.1 ± 0.0	
Academy of Sciences	-1.0 ± 0.1	-1.1 ± 0.1	94%	+0.1 ± 0.0	+0.1 ± 0.0	95%
Vavilov	-0.2 ± 0.0	-0.3 ± 0.0	94%	+0.1 ± 0.0	+0.1 ± 0.0	87%
Albanov	0.0 ± 0.0			0.0 ± 0.0	0.0 ± 0.0	83%
Pioneer	0.0 ± 0.0			0.0 ± 0.0	0.0 ± 0.0	82%
Rusanov	-0.2 ± 0.0	-0.1 ± 0.0	87%	-0.1 ± 0.0	-0.1 ± 0.0	76%
Karpinsky	-0.1 ± 0.0	-0.2 ± 0.0	84%	+0.1 ± 0.0	+0.1 ± 0.0	79%
University	+0.1 ± 0.0	0.0 ± 0.0	87%	+0.1 ± 0.0	+0.1 ± 0.0	85%
Semenov-Tyan-Shansky + Kropotkin + Leningradsky	-0.2 ± 0.0	0.0 ± 0.0	75%	-0.2 ± 0.0	-0.2 ± 0.0	76%
Sv	-13.3 ± 0.8	-10.8 ± 0.8	85%	-2.5 ± 0.2	-2.5 ± 0.2	69%
Sum GIC and upscale	-13.8 ± 0.4	-11.2 ± 0.4		-2.6 ± 0.1	-2.6 ± 0.1	
Austfonna	-4.6 ± 0.3	-4.6 ± 0.3	98%	0.0 ± 0.0	0.0 ± 0.0	89%
Vestfonna	-0.4 ± 0.0	-0.4 ± 0.0	95%	0.0 ± 0.0	0.0 ± 0.0	90%
Barentsøya	-0.2 ± 0.0	-0.1 ± 0.0	92%	-0.1 ± 0.0	-0.1 ± 0.0	90%
Edgeøya	-0.9 ± 0.0	-0.5 ± 0.0	90%	-0.4 ± 0.0	-0.4 ± 0.0	84%
NW Spitzbergen	-2.7 ± 0.1	-1.9 ± 0.1	77%	-0.8 ± 0.1	-0.8 ± 0.1	58%
NE Spitzbergen	-0.7 ± 0.0	-0.4 ± 0.0	82%	-0.3 ± 0.0	-0.3 ± 0.0	67%
S Spitzbergen	-4.0 ± 0.2	-3.1 ± 0.2	74%	-0.8 ± 0.1	-0.9 ± 0.1	67%
Ic	-2.6 ± 0.2			-1.2 ± 0.1	-2.6 ± 0.2	80%
Sum GIC and upscale	-2.6 ± 0.1			-1.4 ± 0.1	-2.6 ± 0.1	
Vatnajökull	-1.6 ± 0.1			-0.9 ± 0.1	-1.6 ± 0.1	84%
Langjökull	-0.3 ± 0.0			-0.3 ± 0.0	-0.3 ± 0.0	77%
Hofsjökull	-0.2 ± 0.0			-0.1 ± 0.0	-0.2 ± 0.0	84%
Mýrdalsjökull + Eyafjallajökull	-0.1 ± 0.0			+0.1 ± 0.0	-0.1 ± 0.0	63%
Drangajökull	-0.1 ± 0.0			+0.1 ± 0.0	-0.1 ± 0.0	67%
CAA-N	-32.3 ± 1.6	-13.3 ± 0.9	63%	-17.9 ± 1.3	-19.0 ± 1.3	62%
Sum GIC and upscale	-32.6 ± 0.8	-12.9 ± 0.4		-18.0 ± 0.6	-19.7 ± 0.6	
N Ellesmere	-9.4 ± 0.5	-2.7 ± 0.2	56%	-6.0 ± 0.4	-6.7 ± 0.5	57%
Agassiz	-5.0 ± 0.3	-1.5 ± 0.1	52%	-3.1 ± 0.2	-3.5 ± 0.3	64%
Muller	-2.8 ± 0.2	-0.2 ± 0.0	41%	-2.4 ± 0.2	-2.6 ± 0.2	59%
Steacie	-1.8 ± 0.1			-1.6 ± 0.1	-1.8 ± 0.1	50%
Prince of Wales	-5.9 ± 0.3	-4.1 ± 0.3	61%	-1.7 ± 0.1	-1.8 ± 0.1	62%
Sydkap	-0.8 ± 0.0	-0.2 ± 0.0	55%	-0.6 ± 0.0	-0.6 ± 0.0	71%
Manson	-1.7 ± 0.1	-1.4 ± 0.1	71%	-0.3 ± 0.0	-0.3 ± 0.0	53%
Devon	-4.3 ± 0.2	-2.9 ± 0.2	83%	-1.3 ± 0.1	-1.4 ± 0.1	82%
CAA-S	-24.8 ± 1.8	-1.3 ± 0.1	37%	-23.1 ± 1.6	-23.5 ± 1.8	56%
Sum GIC and upscale	-24.5 ± 0.7	-1.5 ± 0.1		-22.7 ± 0.7	-23.0 ± 0.7	
Bylot	-2.3 ± 0.2	-0.2 ± 0.0	67%	-2.2 ± 0.2	-2.1 ± 0.2	54%
Barnes	-4.5 ± 0.3			-4.5 ± 0.3	-4.5 ± 0.3	97%
Penny	-4.3 ± 0.3	-0.8 ± 0.1	11%	-3.5 ± 0.2	-3.5 ± 0.3	44%
N Baffin	-2.3 ± 0.2	-0.2 ± 0.0	39%	-2.0 ± 0.1	-2.1 ± 0.2	51%
Central Baffin	-5.2 ± 0.4	-0.2 ± 0.0	50%	-4.8 ± 0.3	-5.0 ± 0.4	50%
S Baffin	-3.8 ± 0.3			-3.7 ± 0.3	-3.8 ± 0.3	42%
CAA	-57.1 ± 2.4	-14.5 ± 0.9	61%	-41.0 ± 2.1	-42.6 ± 2.2	60%
RAA	-14.0 ± 0.5	-10.5 ± 0.5	87%	-3.1 ± 0.2	-3.5 ± 0.2	77%
BKS	-27.3 ± 0.9	-21.3 ± 0.9	86%	-5.6 ± 0.3	-6.0 ± 0.3	73%
Total Arctic	-87.0 ± 2.6	-35.8 ± 1.3	74%	-47.8 ± 2.1	-51.2 ± 2.3	64%

Table S2 | Summary table of *partitioned mass budget, and SMB anomaly model coefficients*: the dynamic mass budget is calculated with a constant density of ice equal to 850 kg m^{-3} . Area-specific D and SMB are computed relative to the total marine/land-terminating basin area (*) and relative to the total glaciated area (**) of each region. Numbers in brackets under region names indicate the values of lat_ts and lon_0 of the local polar stereographic projection used to calculate the \dot{h} maps and hence corresponding to the x and y components of the SMB anomaly model.

Region	Mass budget [$\text{kg m}^{-2} \text{ a}^{-1}$]	D_{spec} [$\text{kg m}^{-2} \text{ a}^{-1}$]*	D_{spec} [$\text{kg m}^{-2} \text{ a}^{-1}$]**	SMB_{spec} [$\text{kg m}^{-2} \text{ a}^{-1}$]**	SMB anomaly model polynomial coefficients [$1\text{e}^{-3} \text{ a}^{-1}$]				
					a_0	a_1	a_2	a_3	a_4
FJL [80.5 55]	-297 ± 23	-235 ± 54	-212 ± 49	-84 ± 44	1.7e^{-5}	-1.4e^{-2}	4.5	1.4e^{-3}	2.0e^{-3}
NZ [75.5 61]	-385 ± 18	-82 ± 37	-51 ± 29	-331 ± 21	-2.9e^{-6}	4.2e^{-3}	-0.5	1.7e^{-3}	0.3e^{-3}
SZ [79.5 99]	-106 ± 6	-205 ± 20	-98 ± 11	-9 ± 8	-7.3e^{-7}	-1.6e^{-3}	2.0	-1.0e^{-3}	0.2e^{-3}
Sv [78.5 20]	-401 ± 24	-277 ± 41	-188 ± 30	-214 ± 18	6.3e^{-7}	-2.9e^{-3}	3.8	1.4e^{-3}	1.6e^{-3}
Ic [65 -19]	-231 ± 16	-	-	-231 ± 16	-	-	-	-	-
CAA-N [79 -84]	-308 ± 15	$+7 \pm 28$	$+3 \pm 23$	-311 ± 17	-5.3e^{-7}	2.0e^{-3}	-2.0	0.1e^{-3}	-0.2e^{-3}
CAA-S [70 -73]	-606 ± 44	$+93 \pm 137$	$+7 \pm 63$	-613 ± 44	-4.2e^{-7}	1.3e^{-3}	-0.6	4.8e^{-5}	0.6e^{-3}
RAA	-275 ± 10	-164 ± 25	-106 ± 18	-168 ± 15	-	-	-	-	-
BKS	-325 ± 11	-210 ± 22	-139 ± 16	-185 ± 11	-	-	-	-	-
Total Arctic	-361 ± 11	-102 ± 17	-46 ± 16	-319 ± 16	-	-	-	-	-

Table S3. Anomalies in sea surface temperature (Δ SST), subsurface ocean temperature (Δ SOT), air temperature (Δ T2m), and sea ice concentration (Δ SIC) during the survey period (2010-2017) relative to the previous two decades (1990-2009). SST and T2m data are from ERA-Interim ; SOT data are from TOPAZ ; SIC data are from NASA bootstrap/team.				
Region	DSST	DSOT	DT2m	DSIC1
	C	C	C	%
FJL	0.3	0.3	3.4	-16.8
NZ	0.8	0.6	2.7	-12.3
SZ	0.2	0.1	2.8	-8.6
Sv	0.9	0.7	2.1	-12.8
Ic	0.1	0.3	0.9	-0.1
CAA-N	0.1	-0.2	0.9	-1.4
CAA-S	0.2	-0.2	2.4	-2.1
RAA	0.5	0.4	2.9	-12.2
BKS	0.6	0.5	2.6	-12.4
CAA	0.1	-0.2	1.3	-1.5

Figure S1 | Coverage of surface elevation change \dot{h} along ice margins with extreme topography: example of Trinity-Wykeham Glacier, Nunavut, Canada. ICESat (left panel) for reference, and CryoSat-2 (right panel). Adapted from Harcourt et al., (2019).



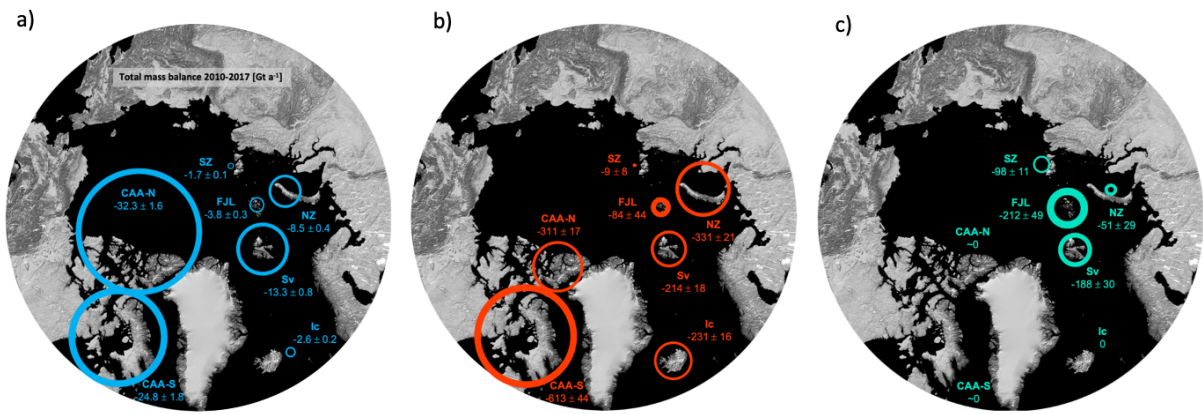
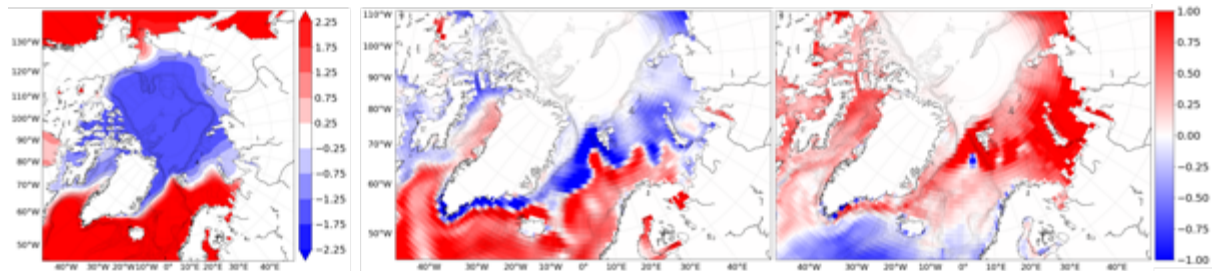


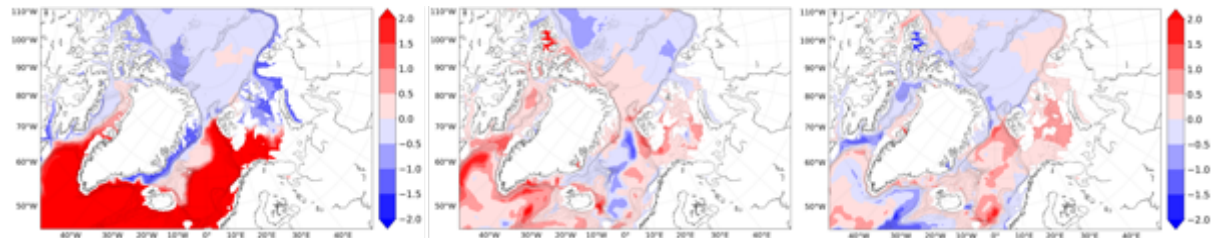
Figure S2 | A map of the Arctic shows the location of GIC and estimates of mass balance from the present study represented by circles with size proportional to ice mass losses and their width proportional to the corresponding error budget. Total mass balance in [Gt a^{-1}] a); and area-specific mass balance in [$\text{kg m}^{-2} \text{a}^{-1}$]: *SMB* b), and *D* c), derived from CryoSat-2.

Figure S3a | SST decadal anomalies (ERA-Interim)



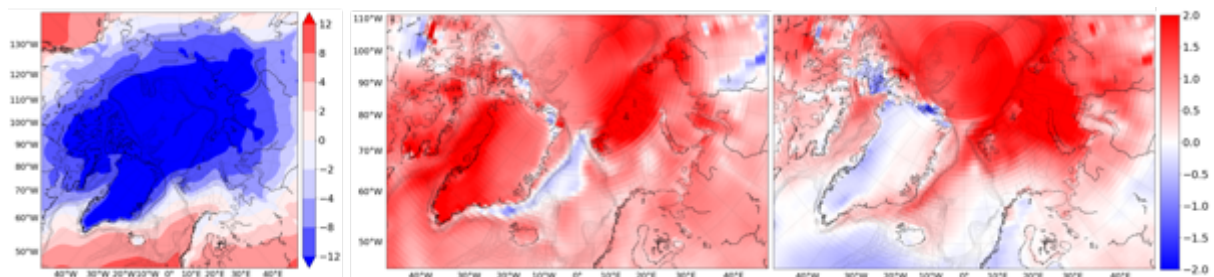
Left: SST decadal mean of annual means (°C) for the 1990-1999 (reference) period. **Middle:** α_1 SST anomaly (°C) between the 2000-2009 and the reference period. **Right:** α_2 SST anomaly (°C) between 2010-2017 and 2000-2009.

Figure S3b | SOT decadal anomalies (TOPAZ)



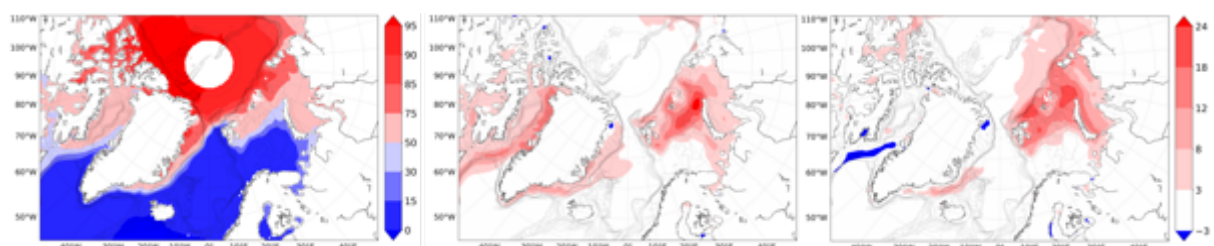
Left: SOT decadal mean of annual means (°C) for the 1990-1999 (reference) period. **Middle:** α_1 SOT anomaly (°C) between the 2000-2009 and the reference period. **Right:** α_2 SOT anomaly (°C) between 2010-2017 and 2000-2009.

Figure S3c | T_{2m} decadal anomalies (ERA-Interim)



Left: T_{2m} decadal mean of annual means (°C) for the 1990-1999 (reference) period. **Middle:** α_1 T_{2m} anomaly (°C) between the 2000-2009 and the reference period. **Right:** α_2 T_{2m} anomaly (°C) between 2010-2017 and 2000-2009.

Figure S3d | SIC decadal anomalies (NASA Team)



Left: SIC decadal mean of annual means (%) for the 1990-1999 (reference) period. **Middle:** α_1 SIC anomaly (%) between the 2000-2009 period and the reference period. **Right:** α_2 SIC anomaly (%) between 2010-2017 and 2000-2009. Positive SIC designate declining sea ice concentrations.

Figure S4 | Validation of CryoSat-2 rates of surface elevation change \dot{h} against OIB: Barnes Ice Cap (top panels), and the Devon Ice Cap (bottom panels) with differences of $0.05 \text{ m a}^{-1} \pm 0.26 \text{ m a}^{-1}$ and $0.00 \text{ m a}^{-1} \pm 0.13 \text{ m a}^{-1}$ respectively for Barnes and Devon Ice Caps.

